frontiers | Frontiers in Earth Science

TYPE Original Research
PUBLISHED 25 July 2025
DOI 10.3389/feart.2025.1632300

OPEN ACCESS

EDITED BY
Jiawang Ge,
Southwest Petroleum University, China

REVIEWED BY
Gemma Aiello,
National Research Council (CNR), Italy
Changan Shan,
Xi'an Shiyou University, China
Xiaosong Wei,
China University of Geosciences
Wuhan, China

*CORRESPONDENCE
Jinjie Yong,
jay_1201@126.com
Shaoyong Hu,
63732060@qq.com
Zhicheng Liu,
lzc_15@126.com

RECEIVED 20 May 2025
ACCEPTED 16 July 2025
PUBLISHED 25 July 2025

CITATION
Yong J, Hu S, He J, Liu Z, Zheng M, Luo P, Liu X and Dong W (2025) Astronomical control on upper ordovician – lower silurian organic matter enrichment in South China. *Front. Earth Sci.* 13:1632300. doi: 10.3389/feart.2025.1632300

Astronomical control on upper ordovician – lower silurian organic matter enrichment in South China

Jinjie Yong*, Shaoyong Hu*, Jie He, Zhicheng Liu*, Mengtian Zheng, Peng Luo, Xin Liu and Wei Dong

Sichuan Institute of Land Science and Technology (Sichuan Satellite Application Technology Center), Chengdu, China

Astronomical forcing governed Late Ordovician–Early Silurian climate dynamics, yet high-resolution Astronomical Time Scales (ATS) and organic enrichment mechanisms during the end-Ordovician extinction remain poorly constrained. In this study, we integrated gamma ray (GR), $\delta^{13}C_{org}$, and chemical index of alteration (CIA) data from the Wufeng–Longmaxi formations (Weimohani section, South China) to establish a floating ATS tuned to 405-kyr eccentricity cycles, anchored to a Hirnantian U–Pb age (444.2 ± 1.6 Ma). This ATS constrains key stage durations (Hirnantian: 1.31 Myr; 432.19–444.01 Ma span) and confirms orbital control on eustasy: 1.2-Myr obliquity paced third-order icehouse-greenhouse transitions, while 405-kyr eccentricity drove fourth-order sea-level fluctuations. The CIA records demonstrate that obliquity-modulated thermohaline circulation enhanced nutrient flux to the Yangtze Shelf, with peak organic enrichment occurring during transitional climates ($\delta^{13}C_{org}$ minima plus CIA maxima) rather than glacial extremes. These findings reveal a eustatic (orbital) dominance over tectonic controls and resolve the synergistic productivity-preservation balance governing organic matter accumulation.

KEYWORDS

astronomical cycles, organic matter enrichment, astronomical timescale, sea-level change, thermohaline circulation, late ordovician extinction

1 Introduction

The Late Ordovician mass extinction (LOME, ~445 Ma) stands as one of the most severe biotic crises in Earth's history, eliminating approximately 85% of marine species (Hu et al., 2021; Ni et al., 2024; Lu et al., 2025). This catastrophic event was driven by a complex interplay of factors, primarily the expansion of Gondwanan ice sheets, widespread marine anoxia, and rapid, volatile climate shifts. A prominent geological signature of this critical interval is the global deposition of organic-rich black shales, which represent significant petroleum source rocks today. Among these, the exceptionally preserved and laterally extensive deposits within the Upper Ordovician Wufeng Formation and the Lower Silurian (Llandovery) Longmaxi Formation on the Yangtze Block of South China provide unparalleled, high-resolution marine archives of contemporaneous oceanic and climatic perturbations (Zhang et al., 2020).

Astronomical forcing, the cyclical variations in Earth's orbit (eccentricity) and axial tilt (obliquity and precession), is increasingly recognized as a fundamental pacemaker of Paleozoic climate dynamics (Herbert, 1991; Berger and Loutre, 1992; Laskar et al., 2004; Hinnov et al., 2018). These Milankovitch cycles modulate insolation patterns, driving icehouse-greenhouse transitions, influencing ocean circulation, and perturbing the global carbon cycle on timescales of tens to hundreds of thousands of years (e.g., Laskar et al., 2004; Hofmann and Wagner, 2011; Li et al., 2016a; Lu et al., 2019a; b; Zhang et al., 2020). Consequently, these orbital rhythms are faithfully encoded in the sedimentary record, offering the potential to construct high-resolution astronomical time scales (ATS) and decipher the chain of Earth system responses.

Despite the recognized importance of astronomical forcing, significant challenges remain. While orbital cycles have been identified within Late Ordovician–Early Silurian strata globally (e.g., Crick et al., 2001; Nestor et al., 2003; Svensen and Hammer, 2015; Lu et al., 2019a; b), high-resolution, well-constrained astronomical time scale (ATS) for the Katian to Telychian stages (encompassing the LOME and its aftermath) are still scarce. This scarcity limits our ability to precisely correlate events, quantify process rates, and establish the exact sequence of environmental changes across this critical boundary. Furthermore, the specific geological mechanisms by which these orbital cycles influenced paleoenvironmental conditions and ultimately controlled the enrichment of organic matter (OM) within these globally significant black shales, particularly during the intense climatic fluctuations of the end-Ordovician, remain unresolved. Understanding this link is crucial for unraveling the complex feedbacks between orbital forcing, climate, ocean chemistry, and biotic turnover during mass extinctions.

To address these knowledge gaps, this study focuses on a continuous marine succession of the Wufeng-Longmaxi formations at Weimohani section, Sichuan Province, China (Figure 1). We present a high-resolution, multi-proxy dataset including gamma ray (GR) logging, $\delta^{13}C_{org}$, and the chemical index of alteration (CIA). Our primary objectives are to: (1) construct an astronomical time scale for the Katian–Telychian interval by identifying and tuning Milankovitch cycles within the sedimentary record; (2) elucidate the expression of orbital forcing on Late Ordovician–Early Silurian climate dynamics, particularly icehouse-greenhouse transitions, as recorded by geochemical proxies; and (3) determine the mechanisms through which astronomical cycles governed organic matter enrichment. By integrating cyclostratigraphic analysis with chemostratigraphic stratigraphic approaches, this study aims to provide new constraints on the pacing and drivers of environmental change during a pivotal chapter in Earth's history.

2 Geological setting

The collision between the Yangtze Block and the Cathaysia Block led to the emergence of several key paleogeographic features: the Chuanzhong Uplift in the northwest, the Kangdian and Qianzhong Uplift in the south, and the Xuefeng Submarine High (Shan et al., 2017; Zhang et al., 2020) (Figures 1A–C). During the Hirnantian, continued convergence drove the expansion of the Chuanzhong, Kangdian, and Qianzhong Uplift areas while simultaneously inducing subsidence within the Yangtze Block basement. Despite this regional subsidence, global glaciation events caused eustatic sea level to fall at a rate exceeding the subsidence (Cherns and Wheeley, 2007; Delabroye and Vecoli, 2010; Lu et al., 2019a; b; Zhang et al., 2023). Consequently, sedimentary environments recorded in the Upper Ordovician Wufeng Formation (Katian to early Hirnantian) and the overlying Lower Silurian Longmaxi Formation (late Hirnantian to Telychian) transitioned progressively from distal to proximal shelf settings (Wang et al., 2019; Shu et al., 2019). This succession preserves abundant and well-documented graptolite fossils (Zhu et al., 2018; Zhang et al., 2020).

The Wufeng Formation comprises the graptolite biozones *Dicellograptus complexus* (Lower Subzone), *Tangyagraptus typicus, Diceratograptus mirus*, and *Normalograptus extraordinarius* (Katian -early Hirnantian). The Longmaxi Formation includes the *Persculptograptus persculptus* to *Coronograptus cyphus* zones (Rhuddanian), followed by the *Demirastrites triangulatus*, *Lituigraptus convolutus*, and *Stimulograptus sedgwickii* zones (Aeronian), and the *Spirograptus guerichi* zone (Telychian) (Chen et al., 2000; 2015).

The Weimohani section is located in the southwestern Yangtze Block, within the Xichang Basin of South China. During the Late Ordovician (Katian) to Early Silurian (Telychian) interval, this region occupied a low to middle palaeolatitude position. (Metcalfe, 1994; Zhong et al., 2018; Wu et al., 2024; Bao et al., 2025; Figures 1A,B). This succession has been thoroughly investigated using integrated biostratigraphy and carbon isotope stratigraphy. It comprises black shales with thin limestone interlayers (Hirnantian), black shales with calcareous mudstone interlayers (Katian to Aeronian), as well as yellow-grey shales with thin siltstone calcareous interlayers (Telychian) (Figure 2).

3 Materials and methods

3.1 Climatic proxies

Natural GR, organic carbon isotope $\delta^{13}C_{org}$, and CIA were employed as paleoclimatic proxies in this study. High-resolution (0.1 m interval) GR measurements were acquired directly from outcrop using a XTG-2000M Digital GR Spectrometer. This instrument detects natural gamma-ray radioactivity emitted by potassium (K), uranium (U), and thorium (Th) isotopes during decay. GR intensity primarily reflects the abundance of clay minerals, organic matter, and shale (Wei et al., 2020; 2023). Specifically, K is predominantly hosted in clay minerals, mica, and chloride salts (Schnyder et al., 2006; Tenchov, 1997; Liu et al., 2019). U is commonly associated with clays, feldspar, heavy minerals, phosphate, and organic matter (Schnyder et al., 2006; Li et al., 2016b; Wei et al., 2023; 2024). Th is concentrated in clays, feldspar, heavy minerals, phosphate, and volcanic ash layers (Schnyder et al., 2006; Li J. L. et al., 2019).

A total of 292 fresh samples were collected from the organic-rich black shale interval of the exposed 36-m-long Weimohani road cut section. Sampling focused on the Katian to Rhuddanian interval (9–27 m depth relative to section base), avoiding weathered surfaces

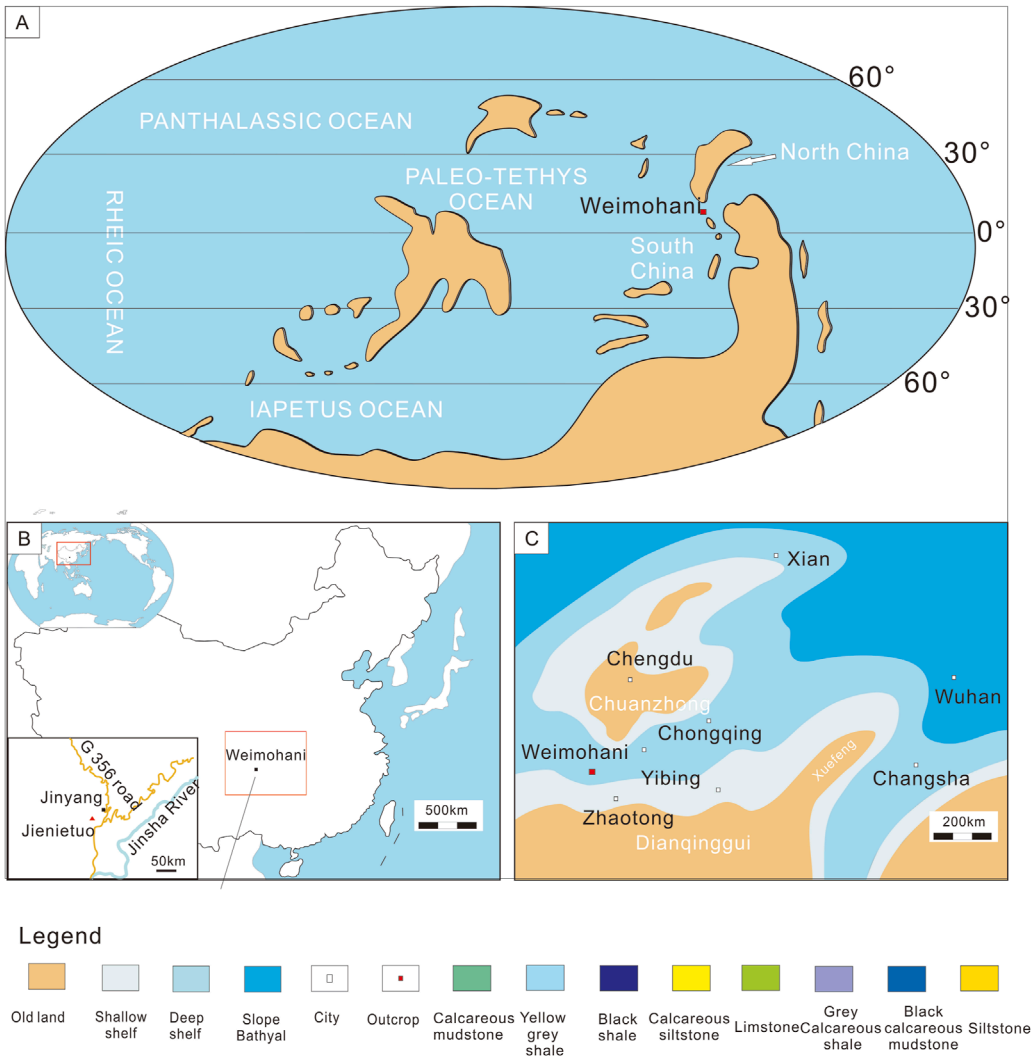

FIGURE 1
(A) Early Silurian paleogeographic reconstruction (modeled using PaleoEarth Lite 1.2, Zhang et al., 2021), depicting the location of the Weimohani section in the Xichang Basin, South China. **(B)** Geographic positioning of the study site within China. **(C)** Depositional facies distribution across the Upper Yangtze region during the Early Silurian (Llandovery epoch, 438–443 Ma).

and outer layers, at intervals of 10–15 cm. Total organic carbon (TOC) contentc, $\delta^{13}C_{org}$ and CIA were conducted at the Sichuan Coalfield Geological Bureau's Testing Center.

3.2 Time-series methods

Cyclostratigraphic analysis was performed using the Acycle software package (v7.0; Li M. et al., 2019), applying the following methods: (1) Data preprocessing: The GR series underwent linear detrending prior to spectral analysis. (2) Spectral analysis: Multi-taper method (MTM) spectral analysis (Thomson, 1982) was applied using three 2π tapers. The significance of spectral peaks potentially representing astronomical cycles was assessed against robust red noise models (85%–99% confidence levels; Mann and Lees, 1996). (3) Evolutionary analysis: Fast Fourier Transform (FFT)-based evolutionary spectrograms were generated to track frequency variations through the section. (4) Sedimentation rate estimation: The correlation coefficient (COCO) and evolutionary correlation coefficient (eCOCO) methods (Li et al., 2018) were used to estimate and track variations in sedimentation rate. (5) Cycle extraction: Gaussian bandpass filtering was employed to isolate specific orbital frequency bands. (6) Astronomical target periods: Due to the chaotic diffusion of the Solar System (Laskar et al., 2004), theoretical astronomical periods for the study interval (~442 Ma) were adopted from Waltham (2015). These target periods include short eccentricity (~100 kyr) and obliquity (~34 kyr). (7) Sea level analysis: Katian–Telychian sea-level variations were quantified using the DYNOT and ρ1 sedimentary noise models (Li et al., 2018). (8) Floating astronomical time scale (ATS) construction: Dominant 405-kyr eccentricity cycles were identified in the GR series (Gaussian bandpass filter: 0.09 ± 0.002 cycles/m) and extracted. These filtered cycles were aligned with a synthetic 405-kyr sinusoidal signal to establish a floating ATS. The floating ATS was anchored to absolute

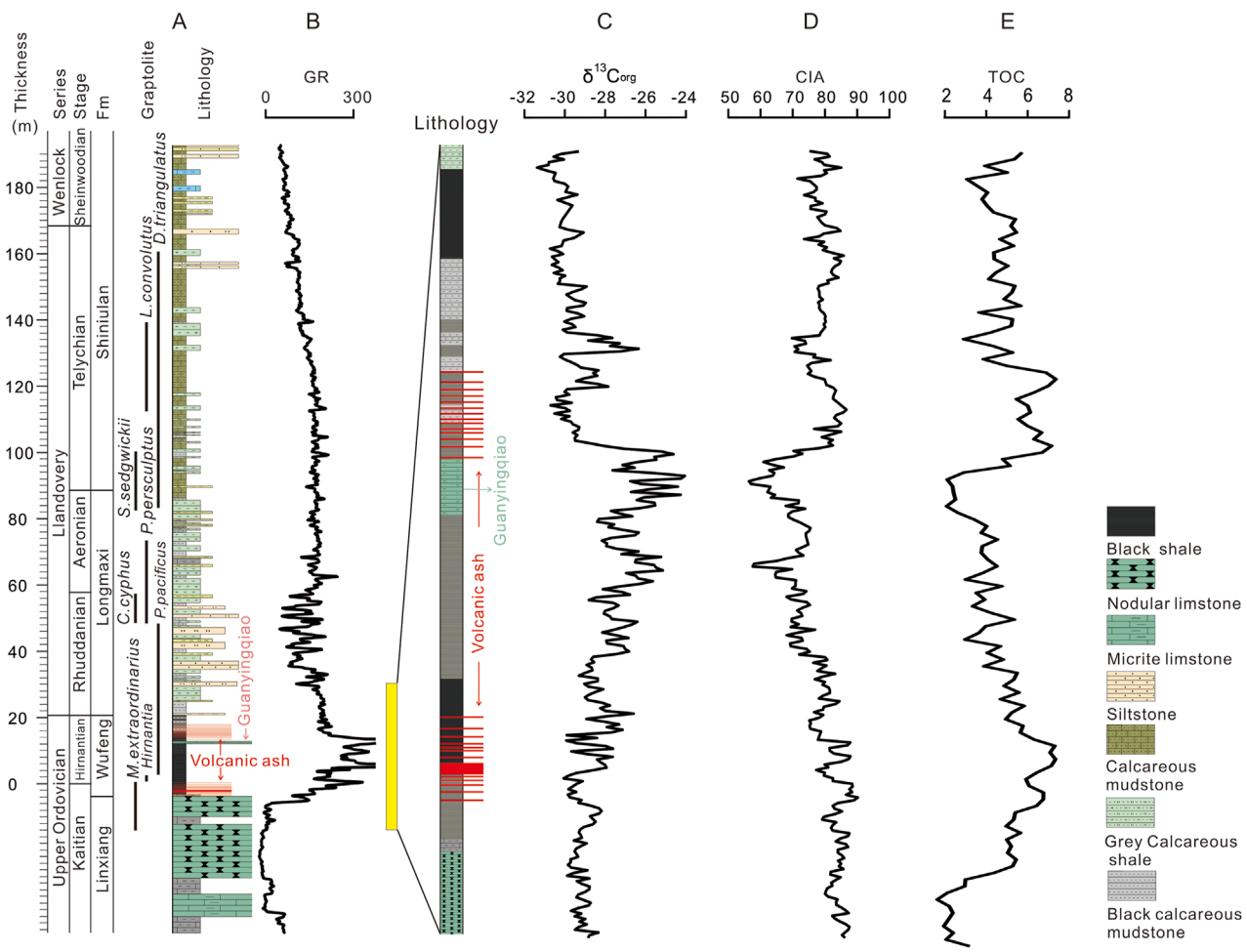

FIGURE 2
Stratigraphy of the Weimohani section interval spanning from the Kaitian to Sheinwoodian stages in the depth (meters) domain. **(A)** Lithological stratigraphy and biostratigraphy. **(B–E)** GR, $\delta^{13}C_{org}$, CIA, and TOC series.

time by tuning the filtered GR cycles to the Hirnantian Guanyinqiao bentonite layer, dated by U-Pb at 444.2 ± 1.6 Ma (Hu et al., 2008). This fixed age point enabled the conversion of depth-domain proxy series (GR, $\delta^{13}C$, CIA) to the time domain (Figure 3B). (9) Analysis of $\delta^{13}C$ and CIA series: The $\delta^{13}C$ and CIA series from the Katian to Rhuddanian interval (−9 to 27 m) were analyzed using the same spectral and filtering methodologies applied to the GR data, integrated within the established ATS.

4 Results

4.1 Spectral analysis in depth domain

The Weimohani outcrop exhibits pronounced sedimentary cyclicity in both lithology and GR data (Figure 3). Distinct lithological rhythms are particularly well-defined in the upper Telychian–Sheinwoodian interval (140–193 m), characterized by alternating argillaceous siltstone–mudstone layers (Figure 4). The middle Rhuddanian–Telychian interval (24–140 m) consists of interbedded silty mudstone and calcareous mudstone sequences, while the Katian–Rhuddanian interval (−5–24 m) comprises cyclic limestone–black mudstone–shale deposits.

GR cyclicity in the Telychian–Sheinwoodian interval (140–193 m) displays dominant wavelengths of ~11.8 m, ~3.1 m, and ~1.2 m. At an average sedimentation rate of 3 cm/kyr, these wavelengths correspond to the 405-kyr (long eccentricity), ~100-kyr (short eccentricity), and 34-kyr (obliquity) Milankovitch cycles, respectively. Similarly, the Rhuddanian–Telychian interval (24–140 m) reveals ~16.0 m, ~3.6 m, and ~1.6 m cycles, aligning with 405-kyr, ~91-kyr, and 35-kyr cycles. The Katian–Rhuddanian interval (−5–24 m) exhibits ~9.2 m and ~2.9 m cycles, reflecting 405-kyr and ~100-kyr cycles (Figure 3A). The $\delta^{13}C_{org}$ series (−9–27 m) shows cycles of ~6.5 m, ~1.7 m, and ~0.65 m corresponding to 405-kyr, 100-kyr, and 35-kyr periods, while the CIA series displays ~6.4 m, ~1.6 m, and ~0.63 m cycles, matching 405-kyr, 100-kyr, and 34-kyr cycles (Figure 3B). In addition, COCO and eCOCO analyses indicate a sedimentation rate of ~3–4 cm/kyr (Figure 4), confirming the reliability of the identified astronomical periodic signals.

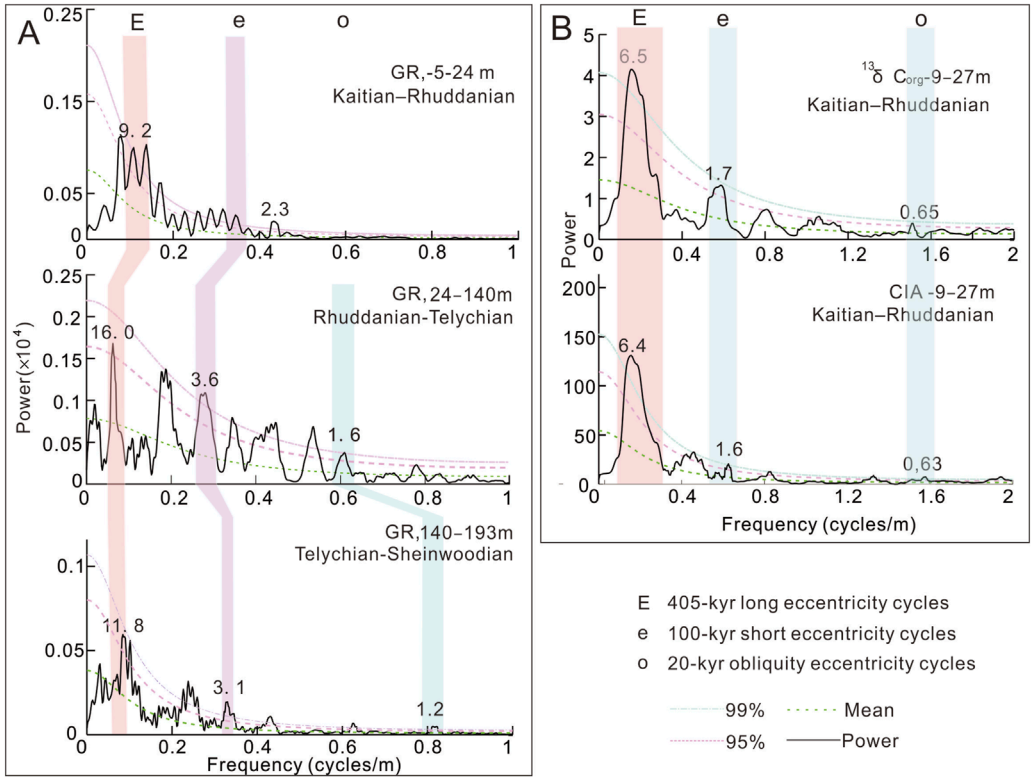

FIGURE 3
Spectral analysis results, plotted alongside a robust red-noise model generated via linear regression and a 20% median-smoothed window (Mann and Lees, 1996). **(A)** 2π MTM power spectra of untuned GR data from Weimohani intervals (–5–193 m) with consistent sedimentation rates, analyzed using a 35% weighted average. **(B)** Detrended $\delta^{13}C_{org}$ and CIA_{corr} spectra (Zhang et al., 2021) from the –9–27 m interval (Rhuddanian–Katian), processed with identical weighting.

4.2 Astronomical tuning

The 405-kyr eccentricity cycle has remained consistent over the past 250 million years (e.g., Laskar et al., 2004; Hinnov and Hilgen, 2012) and has been further validated in the Late Ordovician–Early Silurian strata (Crick et al., 2001; Nestor et al., 2003; Svensen and Hammer, 2015; Lu et al., 2019a). This invariant cycle served as the primary calibration reference for constructing a high-resolution age model. Although limited high-precision astronomical tuning work has been carried out in the Sichuan Basin of China, it has mainly focus on the eastern part of the basin (Lu et al., 2019a), with no such framework yet established for the southwestern region.

Spectral analysis of the 405-kyr-tuned GR series identifies prominent orbital parameters, including peaks corresponding to 405-kyr eccentricity, ~100-kyr short eccentricity, and 36-kyr obliquity (Figure 3B). Orbital signals in the GR, $\delta^{13}C_{org}$, and CIA series were isolated via Gaussian bandpass filtering, revealing ~10 obliquity big cycles (~1.2 Myr) and 30 eccentricity cycles (~405 kyr) spanning the Hirnantian–Telychian interval. By anchoring to the Hirnantian Guanyinqiao U-Pb date (443.2 ± 1.6 Ma; Hu et al., 2008) and correlating with graptolite biozones (Figures 5A,B), stage durations were calculated as follows: Hirnantian (1.31 Myr; 442.70–444.01 Ma), Rhuddanian (2.91 Myr; 439.78–442.70 Ma), Aeronian (2.44 Myr; 437.35–439.78 Ma), and Telychian (5.16 Myr; 432.19–437.35 Ma) (Figures 6A,B). These astronomically derived estimates are consistent with results from previous studies (Ogg et al., 2016; Lu et al., 2019a; Zhong et al., 2019).

5 Discussion

5.1 Orbital-driven climatic changes and sea-level fluctuations

The interplay between astronomical orbital cycles and Earth's climate system fundamentally shaped the environmental conditions for organic matter accumulation during the Late Ordovician-Early Silurian in the Middle-Upper Yangtze region.

5.1.1 CIA as a tracer of orbital-scale climate rhythms

The CIA serves as a robust proxy for paleoclimate variations, closely linked to orbital forcing, reflecting chemical weathering intensity and climatic regimes (Nesbitt and Young, 1982; Fedo et al., 1997). In the Weimohani section, CIA values of 75–85 in the Lower Rhuddanian, Upper Hirnantian, and Upper Katian strata exceed typical shale averages (70–75) (Figure 7), reflecting intense chemical weathering under hot and humid greenhouse conditions, consistent with $\delta^{13}C$ and $\delta^{18}O$ evidence. Conversely, CIA values of 50–70 in the Hirnantian Guanyinqiao Member, analogous to

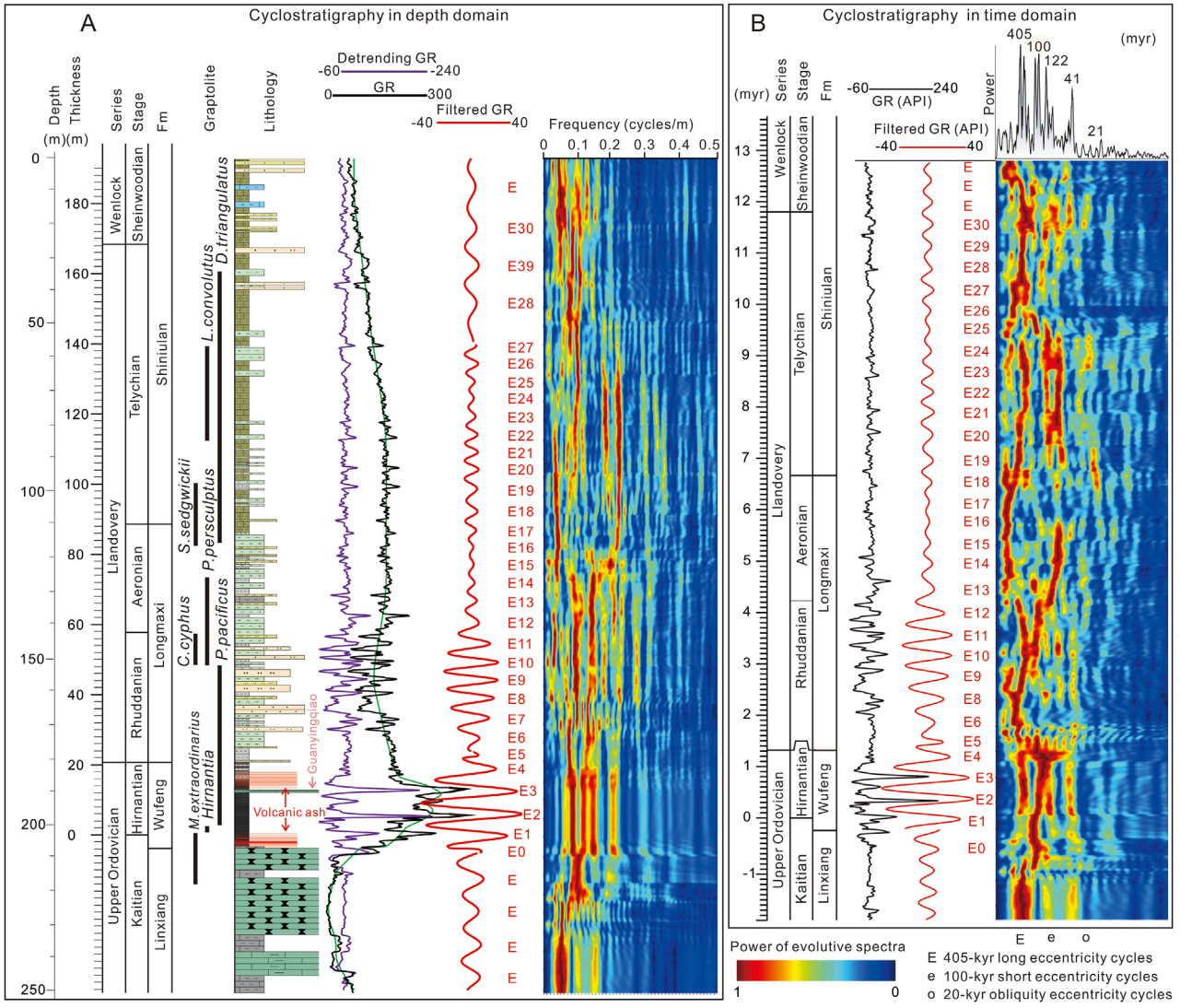

FIGURE 4
Cyclostratigraphic analysis of the Weimohani section (Sichuan Province, South China). **(A)** Depth-domain stratigraphy integrating graptolite biozones (Wufeng, Longmaxi, and Shiniulan formations) to demarcate stage boundaries. A stratigraphic framework for the Upper Ordovician–Lower Silurian was constructed by correlating black shale graptolites with the JY1 well (Chen et al., 2015). The GR series (black line) and 30% weighted average trend (green line) are displayed. Adaptive FFT analysis (60-m sliding window; colored spectrum) identifies 405-kyr eccentricity cycles (red "E" curve, Gaussian-filtered with passbands 0.09 ± 0.002, 0.18 ± 0.05, and 0.15 ± 0.025 cycles/m for intervals 140–193 m, 24–140 m, and −5–24 m, respectively). **(B)** Time-domain cyclostratigraphy after calibrating the GR series to 405-kyr cycles. This adjustment involved removing the 30% weighted average trend and integrating the filtered 405-kyr signal (red "E" curve).

Pleistocene glacial deposits, indicate cold and arid icehouse climates. These shifts align with 405 kyr long eccentricity and 1.2 Myr obliquity cycles (Figure 7), confirming orbital control over low-latitude temperature and humidity.

5.1.2 Hierarchical orbital forcing of climate

Orbital precession and eccentricity primarily modulate climatic shifts in equatorial to mid-latitude zones, whereas obliquity governs polar climatic oscillations (Williams, 1991; Laskar et al., 2004; Liu et al., 2019). However, low-latitude obliquity-driven variability has been documented in the Early Triassic (Li et al., 2016a), Cenozoic (Lourens and Hilgen, 1997), Permian (Fang et al., 2016), and Late Ordovician–Early Silurian (Zhong et al., 2019). In the low-paleolatitude Yangtze region (Weimohani section), the GR, $\delta^{13}C_{org}$, and CIA_{corr} series exhibit ~2–3 obliquity cycles (1.2 Myr) and six 405-kyr eccentricity cycles (late Katian–early Rhuddanian; Figure 7). The 1.2-Myr obliquity rhythm arises from Earth-Mars orbital resonance (s3–s4 secular frequencies; Hinnov, 2000), while 405-kyr eccentricity arises from Venus-Jupiter gravitational interactions (g2–g5; Huang, 2014).

Spectral analyses (Multi-taper method) of stratigraphic records reveal distinct orbital periodicities: 405 kyr long eccentricity, 100–113 kyr short eccentricity, 31–33 kyr obliquity, and 20–23 kyr precession. These cycles operate hierarchically: The 1.2 Myr obliquity cycle governs greenhouse-icehouse transitions by modulating high-latitude solar insolation. Obliquity maxima (e.g., Early-Middle Hirnantian) redirect radiation poleward, cooling the Yangtze region, while minima enhance low-latitude

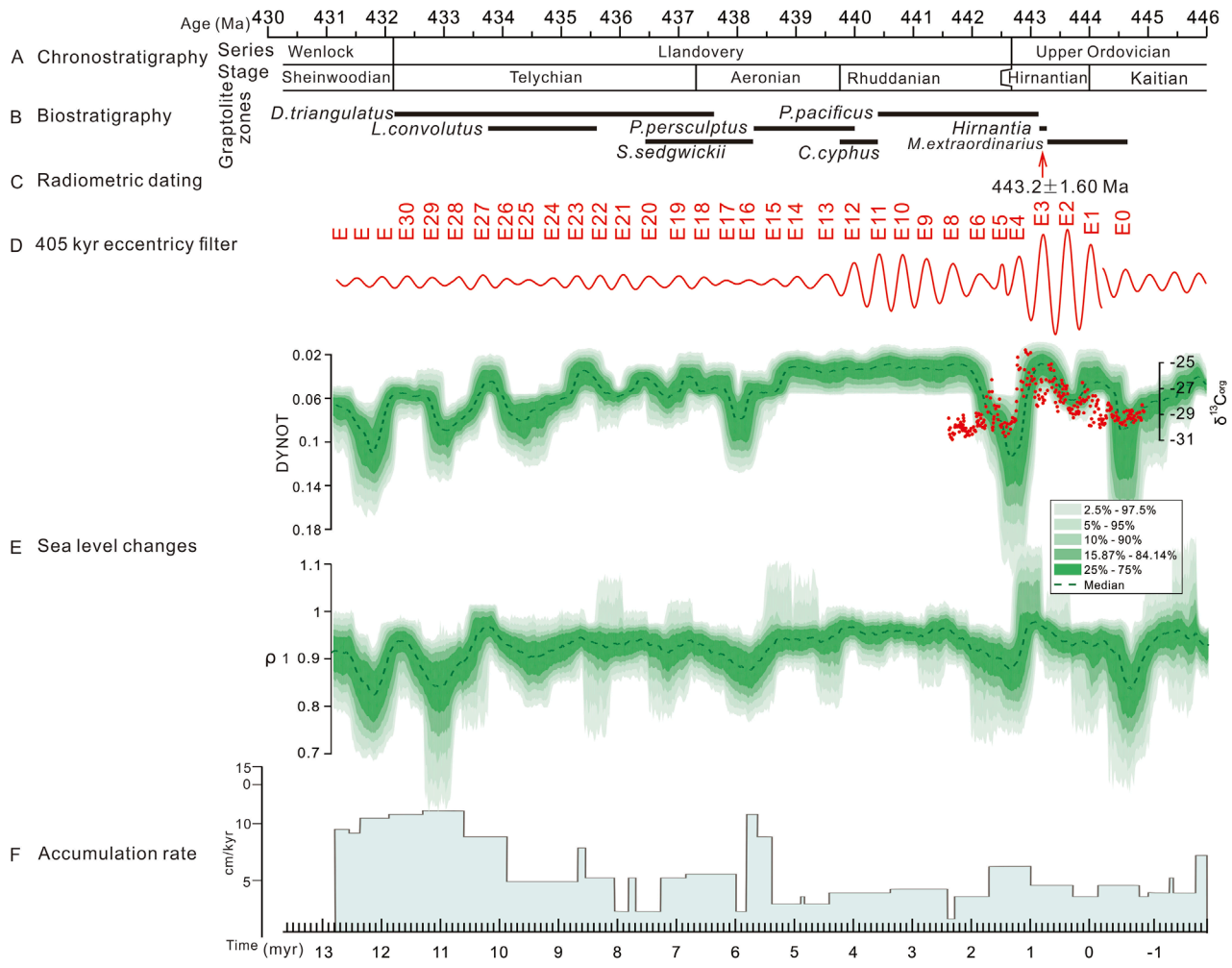

FIGURE 5
Integrated chronostratigraphic synthesis of the Late Ordovician–Early Silurian in South China. **(A,B)**: Chronostratigraphic and biostratigraphic frameworks (modified from Figure 4) delineate stage boundaries using graptolite zones. **(C)**: Radiometric age constraints from Hu et al. (2008) anchor the timeline. **(D)**: 405-kyr eccentricity cycles (correlated with Figure 4). **(E)**: Sea-level trends reconstructed using DYNOT and ρ1 models (Li et al., 2018), aligned with Weimohani $\delta^{13}C_{org}$ records. **(F)**: Sedimentation rates (405-kyr averages) show progressive decline from Katian–Hirnantian to Hirnantian–Rhuddanian, followed by an increase during Aeronian–Telychian (Zhang et al., 2021).

insolation, promoting warming. The 405 kyr eccentricity cycle influences low-latitude seasonality by controlling precession amplitude (Figures 5C,D). Smaller eccentricity values (e.g., Late Katian, Late Hirnantian) dampen seasonality, favoring greenhouse states, whereas larger values (e.g., Early-Middle Hirnantian) amplify seasonality, enhancing icehouse effects. This hierarchical mechanism establishes orbital cycles as the primary driver ("astronomical metronome") of climatic variability.

5.1.3 Orbital-driven sea-level oscillations

Climatic fluctuations caused sea-level fluctuations at different levels through changes in glacier volume and seawater density. The 1.2 Myr obliquity cycle drives third-order sea-level changes, consistent with the trend of the global sea level curve proposed by Haq and Schutter (2008) and Ogg et al. (2016). The 405 kyr long eccentricity cycle controls fourth-order sea-level fluctuations, corresponding to the high-frequency sea-level cycles defined by Loi et al. (2010). For instance, enhanced obliquity amplitude during the Hirnantian glaciation (maxima) triggered polar ice sheet expansion and global sea-level fall. Conversely, diminished obliquity during interglacials (minima) caused ice sheet ablation and sea-level rise (Figures 5E,F). These eustatic changes modulated sedimentary environments (e.g., shallow-to-deep transitions), critically influencing accommodation space and the preservation potential for organic matter.

5.2 Orbital-volcanic coupling and organic matter enrichment

5.2.1 Obliquity-regulated thermohaline circulation

Paleoproductivity and sedimentary preservation are pivotal controls on organic-rich sediment accumulation (Pedersen and Calvert, 1990; Arthur et al., 1998). Nutrients for such sediments derives primarily from continental weathering and fluvial discharge

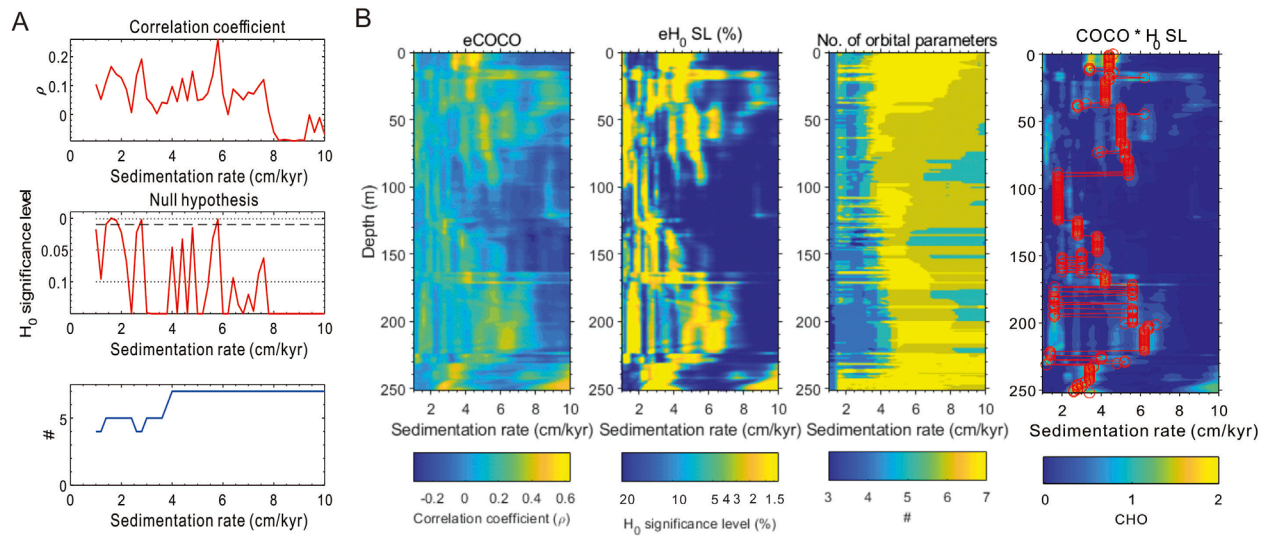

FIGURE 6
COCO and eCOCO analysis results. **(A)** From top to bottom: correlation coefficients, null hypothesis significance level, and number of contributing astronomical parameters involved. **(B)** Evolutionary correlation coefficient, evolutionary H_0 significance level, numbers of contributing astronomical parameters, and correlation coefficient H_0 significance level. The red lines indicate variations in sedimentation rates. Tested sedimentation rates: 0–10 cm/kyr. Monte Carlo simulations: 2000 iterations.

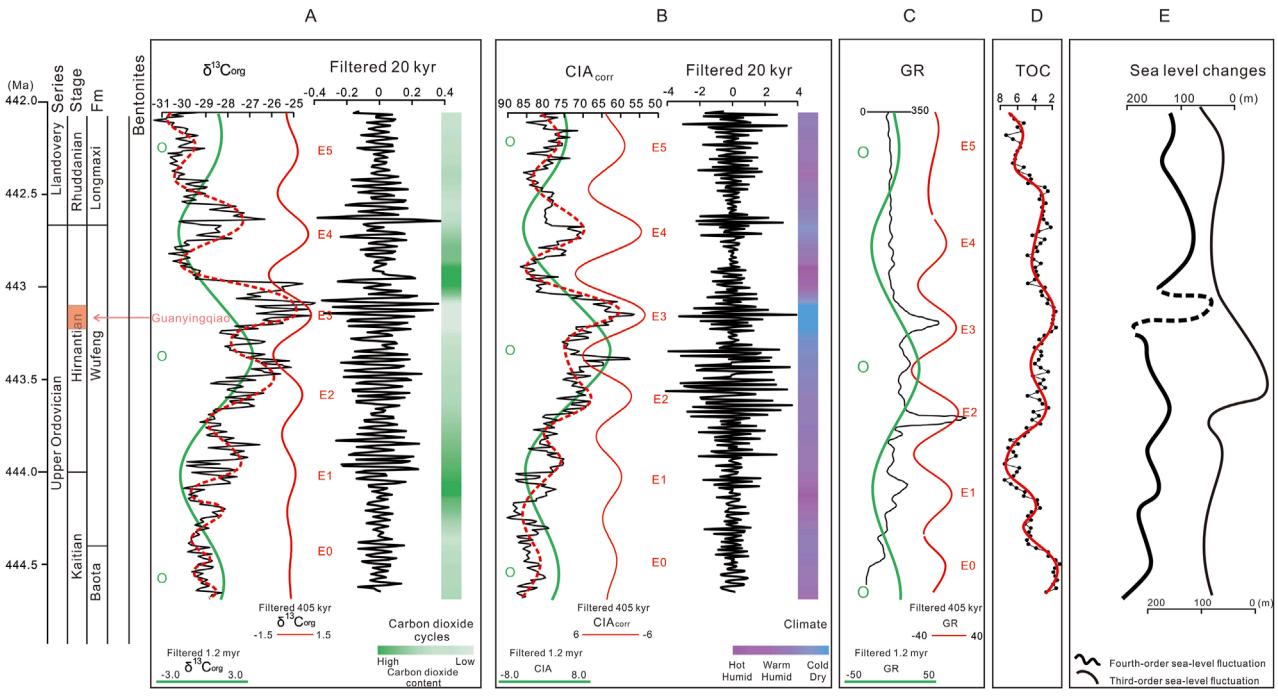

FIGURE 7
Climatic and eustatic variations in the cyclostratigraphic record of the Weimohani section (time domain; Katian–Rhuddanian, −9–27 m). **(A)** $\delta^{13}C_{org}$ series (black line with blue markers). Gaussian-filtered red "E" cycles denote 405-kyr eccentricity; green and light gray lines represent 1.2-Myr obliquity and 20-kyr precession cycles, respectively. Color gradient (green scale) reflects atmospheric carbon dioxide content. **(B)** CIA series (black line). Gaussian-filtered red "E" cycles indicate 405-kyr eccentricity; green and gray lines correspond to 1.2-Myr obliquity and 20-kyr precession. A purple gradient scale denotes climatic phases. **(C)** GR series (black line). Gaussian-derived red "E" cycles mark 405-kyr eccentricity; green cycles indicate 1.2-Myr obliquity. **(D)** TOC series (black line with black markers). Green filtered cycles denote 1.2-Myr obliquity; red dotted cycles align with $\delta^{13}C_{org}$ and CIA_{corr}-derived 405-kyr eccentricity. **(E)** Third-order eustatic sequences (black lines) from other researchers (Haq and Schutter, 2008; Ogg et al., 2016; Loi et al., 2010).

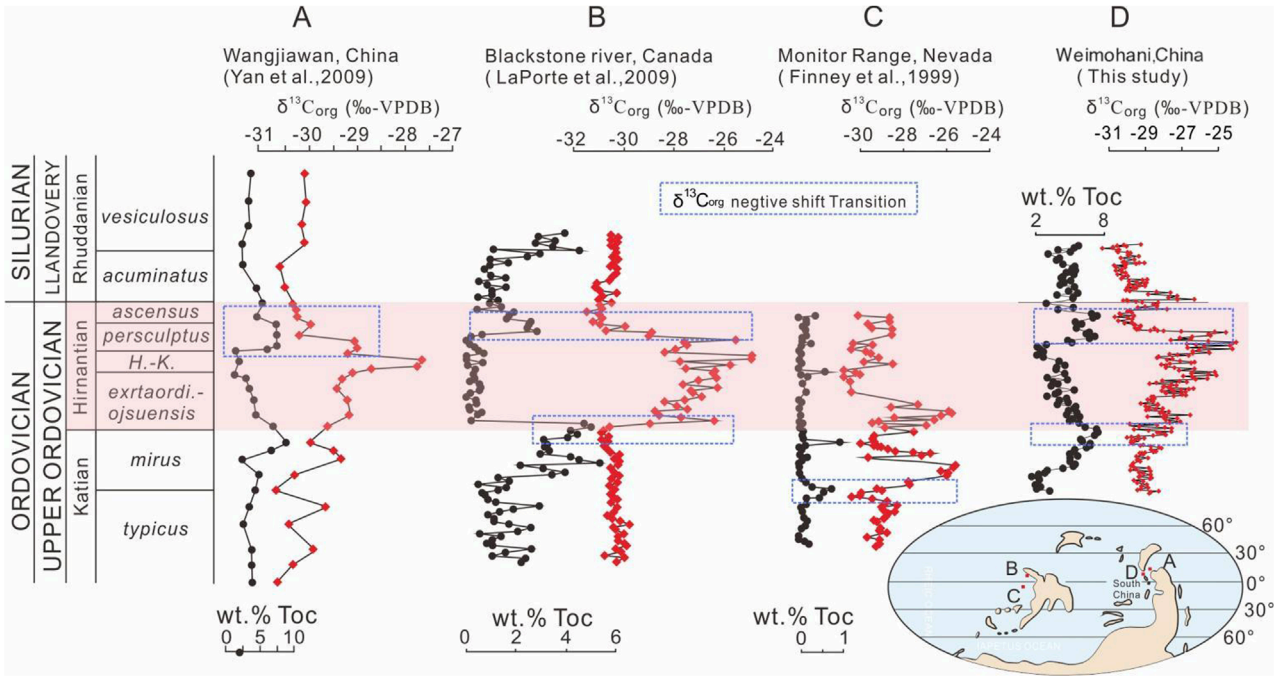

FIGURE 8
Global comparison of organic carbon isotope and TOC profiles across the O-S boundary (Upper Katian through Lower Rhuddanian). **(A)** The Wanjiawan section of Yangtze region, South China. **(B)** The Blackstone River section, Canada (LaPorte et al., 2009). **(C)** The Monitor Range section, Nevada (Finney et al., 1999). **(D)** The Weimohani section of Yangtze region, South China (this study).

(Baumgartner, 2013; Fang et al., 2016), but their distribution is mediated by thermohaline circulation (THC). THC transfers high-latitude climatic forcing to subtropical regions via meridional temperature/density gradients (Fang et al., 2016; 2018) and drives geostrophic bottom currents that transport cold, oxygen-poor, nutrient-laden waters from abyssal zones to surface systems (Broecker, 1991; Talley, 2013).

During the Late Ordovician, the 1.2 Myr obliquity cycle modulates global THC by governing polar ice volume and seawater properties (temperature, salinity, density), thereby influencing nutrient fluxes and productivity (Zhang et al., 2021). Under low obliquity (glacial phases), expanded ice sheets intensified THC and vertical overturning, amplifying bottom currents that channeled nutrient-rich high-latitude waters to the low-latitude Yangtze shelf. This significantly boosted marine primary productivity, evidenced by positive excursions in Ba/Al and Ni/Al ratios. Under high obliquity (interglacial phases), ice sheet ablation weakened THC vigor due to lower sea levels, reducing nutrient supply despite favorable preservation conditions (Fang et al., 2016; Lu et al., 2019a). Productivity declined, resulting in negative shifts in geochemical proxies. Critically, persistently high productivity in volcanic ash-free intervals (e.g., the Lücongpo section during E4) confirms THC as the dominant driver of paleoproductivity.

5.2.2 Synergistic preservation effect of volcanic activity and orbital cycles

Volcanic activity regulated organic matter preservation efficiency by releasing SO_2 and H_2S to form aerosols (Wang et al., 2022), which entered the ocean through acid rain and caused anoxia, but this effect is constrained by orbital cycles. During periods of intense volcanic activity in the Late Katian (E1) and Late Hirnantian (E4), the Jienietuo section in southwestern Sichuan showed Th/U < 2, V/Cr > 4.25, and V/(V+Ni) > 0.6, indicating an anoxic environment with significantly increased TOC content; in contrast, the western Hubei region with weaker volcanic activity had a dysoxic environment and lower TOC during the same period. Notably, the difference in volcanic activity intensity superimposed on orbitally driven sedimentary environment changes led to spatial heterogeneity in organic matter preservation. During the greenhouse period of the 405 kyr eccentricity cycle, the anoxic environment was more stable, amplifying the preservation effect of volcanic activity.

5.2.3 "Orbital-volcanic" coupling model for organic matter enrichment

The enrichment of organic-rich sediments during the Late Ordovician (O-S transition) is governed by the synergistic interplay of orbital cycles and volcanic activity. Orbital forcing—particularly the 1.2 Myr obliquity cycle—regulates productivity via thermohaline circulation (THC)-driven nutrient fluxes, while volcanic ash deposition enhances preservation by intensifying marine anoxia. Vertically, peak organic carbon accumulation occurs in icehouse-greenhouse transition zones (characterized by increasing obliquity and decreasing amplitude), where balanced productivity and preservation optimize TOC. Horizontally, volcanic ash-rich regions (e.g., southwestern Sichuan) form organic enrichment centers due to localized anoxia. This model identifies the Late Katian (E1) and Late Hirnantian (E4) intervals as

prime shale gas targets, where orbital and volcanic drivers coupled optimally.

Obliquity-paced THC critically controls organic accumulation dynamics in the Yangtze region (Lu et al., 2019a; Zhang et al., 2021). Under low obliquity (glacial intervals), intensified THC bottom currents maximize nutrient delivery, but oxygenated low-sea-level conditions limit preservation (Figure 7E). Under high obliquity (greenhouse phases), weakened THC reduces nutrient supply despite anoxic deep waters (Figure 7B). Crucially, transitional intervals exhibit peak TOC enrichment, marked by $\delta^{13}C_{org}$ minima, CIA maxima, and TOC values exceeding those of stable greenhouse phases (Figures 7A,B,D). This transitional optimization, where moderate productivity combines with enhanced anoxia, is corroborated globally (Wanjiawan, Blackstone River, and Monitor Range sections; Finney et al., 1999; Figures 8A–D).

Although sea-level fluctuations and tectonic activity jointly influence sedimentation (Aiello and Budillon, 2004; Aiello and Caccavale, 2023), climate-modulated sea-level changes, acting through THC, dominated O-S transition organic accumulation. Tectonic forcing played a minimal role, evidenced by globally coherent carbon isotope responses to sea-level change. Significant tectonic influence would disrupt this isotopic consistency, confirming THC as the primary control mechanism (Zhang et al., 2021).

6 Conclusion

Three key advances emerge from this study:

A high-resolution floating astronomical time scale (ATS) for the Katian-Telychian (445–432 Ma) was established via 405-kyr GR tuning. The resulting stage durations (Hirnantian: 1.31 Myr) consistent with GTS2016 (Ogg et al., 2016).

Orbital forcing dominated Late Ordovician–Early Silurian paleoclimate dynamics: 1.2-Myr obliquity paced icehouse-greenhouse transitions, while 405-kyr eccentricity governed fourth-order eustasy.

Optimal organic enrichment occurred during obliquity-modulated transitional climates ($\delta^{13}C_{org}$ minima plus CIA maxima), where balanced productivity and preservation maximized TOC accumulation. This transitional enrichment mechanism—reinforced by global analogs—highlights obliquity-paced thermohaline circulation as the primary control, surpassing extremes of high productivity/poor preservation or vice versa. Our approach provides a template for studying organic enrichment in other Paleozoic crises (e.g., Devonian anoxia), with high-resolution $\delta^{13}C_{org}$ and CIA transects offering further insights into productivity-preservation interplay.

Data availability statement

The original contributions presented in the study are included in the article/supplementary material, further inquiries can be directed to the corresponding authors.

Author contributions

JY: Writing – original draft, Writing – review and editing. SH: Writing – review and editing. JH: Writing – review and editing. ZL: Writing – review and editing. MZ: Writing – review and editing. PL: Data curation, Writing – review and editing. XL: Data curation, Writing – review and editing. WD: Data curation, Writing – review and editing.

Funding

The author(s) declare that financial support was received for the research and/or publication of this article. This study was supported by the "Unveiling and Commanding" Project of the Department of Natural Resources of Sichuan Province (Grant No.:2025JDKY0018-10) and the Basic Scientific Research Project of the Sichuan Institute of Land Science and Technology (Grant No.:ZDKJ-2025-001).

Conflict of interest

The authors declare that the research was conducted in the absence of any commercial or financial relationships that could be construed as a potential conflict of interest.

Generative AI statement

The author(s) declare that no Generative AI was used in the creation of this manuscript.

Publisher's note

References

Aiello, G., and Budillon, F. (2004). *Lowstand prograding wedges as fourth-order glacio-eustatic cycles in the pleistocene continental shelf of apulia (southern Italy)*. Special Publications. doi:10.2110/pec.04.81.0215

Aiello, G., and Caccavale, M. (2023). The coastal areas of the Bay of naples: the sedimentary dynamics and geological evolution of the naples canyons. *Geosciences* 13 (8), 226. doi:10.3390/geosciences13080226

Arthur, M. A., Dean, W. E., and Laarkamp, K. (1998). Organic carbon accumulation and preservation in surface sediments on the Peru margin. *Chem. Geol.* 152 (3), 273–286. doi:10.1016/S0009-2541(98)00120-X

Bao, Y. J., Sun, Y. Y., Zhang, D., Yan, J. F., Men, Y. P., Sun, W., et al. (2025). Reducing environment and enhanced productivity controlled the accumulation of organic matter in the upper yangtze basin, south China during the late

ordovician-early Silurian. *J. Asian Earth Sci.* 291, 106694. doi:10.1016/j.jseaes.2025.106694

Baumgartner, P. O. (2013). Mesozoic radiolarites - accumulation as a function of sea surface fertility on tethyan margins and in ocean basins. *Sedimentology* 60 (1), 292–318. doi:10.1111/sed.12022

Berger, A., and Loutre, M. F. (1992). Astronomical solutions for paleoclimate studies over the last 3 million years. *Earth Planet. Sci. Lett.* 111 (2-4), 369–382. doi:10.1016/0012-821X(92)90190-7

Broecker, W. (1991). The great ocean conveyor. *Oceanography* 4 (2), 79–89. doi:10.5670/oceanog.1991.07

Chen, X., Fan, J. X., Zhang, Y. D., Wang, H. Y., Chen, Q., Wang, W. H., et al. (2015). Subdivision and delineation of the wufeng and lungmachi Black shales in the subsurface areas of the yangtze platform. *J. Stratigr.* 39 (4), 352–357.

Chen, X., Rong, J. Y., Mitchell, C. E., Harper, D. A. T., Fan, J., Zhan, R., et al. (2000). Late Ordovician to earliest Silurian graptolite and brachiopod biozonation from the yangtze region, south China, with a global correlation. *Geol. Mag.* 137, 623–650. doi:10.1017/s0016756800004702

Cherns, L., and Wheeley, J. R. (2007). A pre-Hirnantian (late Ordovician) interval of global cooling – the boda event re-assessed. *Palaeogeogr. Palaeoclimatol. Palaeoecol.* 251 (3-4), 449–460. doi:10.1016/j.palaeo.2007.04.010

Crick, R., Ellwood, B., Hladil, J., El, H. A., Hrouda, F., and Chlupac, I. (2001). Magnetostratigraphy susceptibility of the Přídolian–Lochkovian (Silurian–Devonian) GSSP (klonk, Czech Republic) and a coeval sequence in anti-atlas Morocco. *Palaeogeogr. Palaeoclimatol. Palaeoecol.* 167 (1-2), 73–100. doi:10.1016/s0031-0182(00)00233-9

Delabroye, A., and Vecoli, M. (2010). The end-ordovician glaciation and the hirnantian stage: a global review and questions about late Ordovician event stratigraphy. *Earth-Science Rev.* 98 (3-4), 269–282. doi:10.1016/j.earscirev.2009.10.010

Fang, Q., Wu, H., Hinnov, L. A., Tian, W., Wang, X., Yang, T., et al. (2018). Abiotic and biotic responses to Milankovitch-forced megamonsoon and glacial cycles recorded in south China at the end of the late Paleozoic ice age. *Glob. Planet. Change* 163, 97–108. doi:10.1016/j.gloplacha.2018.01.022

Fang, Q., Wu, H., Hinnov, L. A., Wang, X., Yang, T., Li, H., et al. (2016). A record of astronomically forced climate change in a late Ordovician (sandbian) deep marine sequence, ordos basin, north China. *Sediment. Geol.* 341, 163–174. doi:10.1016/j.sedgeo.2016.06.002

Fedo, C. M., Young, G. M., and Nesbitt, H. W. (1997). Paleoclimatic control on the composition of the Paleoproterozoic serpent formation, huronian supergroup, Canada: a greenhouse to icehouse transition. *Precambrian Res.* 86 (3-4), 201–223. doi:10.1016/s0301-9268(97)00049-1

Finney, S. C., Berry, W. B. N., Cooper, J. D., Ripperdan, R. L., Sweet, W. C., Jacobson, S. R., et al. (1999). Late Ordovician mass extinction: a new perspective from stratigraphic sections in central Nevada. *Geology* 27 (3), 215. doi:10.1130/0091-7613(1999)027<0215:lomean>2.3.co;2

Haq, B. U., and Schutter, S. R. (2008). A chronology of Paleozoic sea-level changes. *Science* 322 (5898), 64–68. doi:10.1126/science.1161648

Herbert, T. D. (1991). Long climatic time series from sediment physical property measurements. *J. Sediment. Petrology* 61 (7), 1089–1108. doi:10.1306/d4267843-2b26-11d7-8648000102c1865d

Hinnov, L. (2000). New perspectives on orbitally forced stratigraphy. *Annu. Rev. Earth Planet. Sci.* 28, 419–475. doi:10.1146/annurev.earth.28.1.419

Hinnov, L., and Hilgen, F. J. (2012). "Cyclostratigraphy and astrochronology," in *The geologic time scale*. Editors F. Gradstein, J. Ogg, M. Schmitz, and G. Ogg (Elsevier), 63–83.

Hinnov, L., Rodrigues, P., and Franco, D. (2018). The evolution of a Milankovitch-like spectrum in the banded iron formation of the 2.5 Ga dales gorge member (hamersley basin, Australia).

Hofmann, P., and Wagner, T. (2011). ITCZ controls on Late Cretaceous black shale sedimentation in the tropical Atlantic Ocean. *Paleoceanography* 26 (4). doi:10.1029/2011pa002154

Hu, D., Li, M., Chen, J., Luo, Q., Grasby, S. E., Zhang, T., et al. (2021). Major volcanic eruptions linked to the late Ordovician mass extinction: evidence from mercury enrichment and Hg isotopes. *Glob. Planet. Change* 196, 103374. doi:10.1016/j.gloplacha.2020.103374

Hu, Y. H., Zhou, J. B., Song, B., Wei, L., and Sun, W. D. (2008). Shrimp zircon U-Pb dating of bentonite layers on the top of Ordovician in wangjiawan section, yichang, Hubei, China. *Sci. Sin.* 38 (1), 72–77.

Huang, C. (2014). The current status of cyclostratigraphy and astrochronology in the Mesozoic. *Earth Sci. Front.* 21 (2), 8–66. doi:10.13745/j.esf.2014.02.005

LaPorte, D. F., Holmden, C., Patterson, W. P., Loxton, J. D., Melchin, M. J., Mitchell, C. E., et al. (2009). Local and global perspectives on carbon and nitrogen cycling during the Hirnantian glaciation. *Palaeogeogr. Palaeoclimatol. Palaeoecol.* 276 (1-4), 182–195. doi:10.1016/j.palaeo.2009.03.009

Laskar, J., Robutel, P., Joutel, F., Gastineau, M., Correia, A. C. M., and Levrard, B. (2004). A long-term numerical solution for the insolation quantities of the Earth. *Astronomy Astrophysics* 428 (1), 261–285. doi:10.1051/0004-6361:20041335

Li, J. L., Zhang, T. S., Liang, X., Zhang, J. H., Shu, H. L., Zhang, Z., et al. (2019a). Relation and contribution rate of graptolite to organic matter enrichment in shale: a case study from well YS118 at the southern margin of the sichuan basin. *Nat. Gas. Ind.* 39 (12), 40–45. doi:10.3787/j.issn.1000-0976.2019.12.005

Li, M., Hinnov, L., and Lee, K. (2019b). Acycle: time-series analysis software for paleoclimate projects and education. *Comput. and Geosciences* 127, 12–22. doi:10.1016/j.cageo.2019.02.011

Li, M., Hinnov, L. A., Huang, C., and Ogg, J. G. (2018). Sedimentary noise and sea levels linked to land–ocean water exchange and obliquity forcing. *Nat. Commun.* 9 (1), 1004. doi:10.1038/s41467-018-03454-y

Li, M., Huang, C., Hinnov, L., Ogg, J., Chen, Z., and Zhang, Y. (2016b). Obliquity forced climate during the Early Triassic hothouse in China. *Geology* 44, 623–626. doi:10.1130/G37970.1

Li, M., Ogg, J., Zhang, Y., Huang, C., Hinnov, L., Chen, Z.-Q., et al. (2016a). Astronomical tuning of the end-permian extinction and the Early Triassic epoch of south China and Germany. *Earth Planet. Sci. Lett.* 441, 10–25. doi:10.1016/j.epsl.2016.02.017

Liu, Y., Huang, C. J., Ogg, J. G., Algeo, T. J., Kemp, D. B., and Shen, W. L. (2019). Oscillations of global sea-level elevation during the Paleogene correspond to 1.2-Myr amplitude modulation of orbital obliquity cycles. *Earth Planet. Sci. Lett.* 522, 65–78. doi:10.1016/j.epsl.2019.06.023

Loi, A., Ghienne, J. F., Dabard, M. P., Paris, F., Botquelen, A., Christ, N., et al. (2010). The late Ordovician glacio-eustatic record from a high-latitude storm-dominated shelf succession: the bou ingarf section (antiatlas, southern Morocco). *Palaeogeogr. Palaeoclimatol. Palaeoecol.* 296, 332–358. doi:10.1016/j.palaeo.2010.01.018

Lourens, L. J., and Hilgen, F. J. (1997). Long-periodic variations in the Earth's obliquity and their relation to third-order eustatic cycles and late Neogene glaciations. *Quat. Int.* 40, 43–52. doi:10.1016/S1040-6182(96)00060-2

Lu, Y., Hao, F., Ma, Y., Wei, W., Jun, S., Wang, Y., et al. (2025). Spatial heterogeneity in salinity and redox dynamics during the Ordovician-Silurian transition: multi-proxy constraints on the late Ordovician mass extinction mechanisms. *Chem. Geol.* 690, 122860. doi:10.1016/j.chemgeo.2025.122860

Lu, Y., Huang, C., Jiang, S., Zhang, J., Lu, Y., and Liu, Y. (2019a). Cyclic late katian through Hirnantian glacioeustasy and its control of the development of the organic-rich wufeng and longmaxi shales, south China. *Palaeogeogr. Palaeoclimatol. Palaeoecol.* 526, 96–109. doi:10.1016/j.palaeo.2019.04.012

Lu, Y., Jiang, S., Lu, Y., Xu, S., Shu, Y., and Wang, Y. (2019b). Productivity or preservation? The factorganic-rich sediment controlling the organic matter accumulation in the late katian through hirnantian wufeng organic-rich shale, south China. *Mar. Petroleum Geol.* 109, 22–35. doi:10.1016/j.marpetgeo.2019.06.007

Mann, M. E., and Lees, J. M. (1996). Robust estimation of background noise and signal detection in climatic time series. *Clim. Change* 33, 409–445. doi:10.1007/BF00142586

Metcalfe, I. (1994). Late Palaeozoic and Mesozoic palaeogeography of eastern pangaea and tethys: global environments and resources. *arXiv* 17, 97–111.

Nesbitt, H. W., and Young, G. M. (1982). Early Proterozoic climates and plate motions inferred from major element chemistry of lutites. *Nature* 299, 715–717. doi:10.1038/299715a0

Nestor, H., Einasto, R., Männik, P., and Nestor, V. (2003). Correlation of lower-middle llandovery sections in central and southern Estonia and sedimentation cycles of lime muds. *Proc. Est. Acad. Sci. Geol.* 52, 3–27. doi:10.3176/geol.2003.1.01

Ni, X., Yin, R., Yang, R., Qiao, W., Chen, J., and Gao, J. (2024). Mercury isotopes of the late Ordovician to Middle Triassic tuff layers in south China link the fate of ancient volcanism and the mass extinction. *J. Asian Earth Sci.* 271, 106234. doi:10.1016/j.jseaes.2024.106234

Ogg, J. G., Ogg, G., and Gradstein, F. M. (2016). *A concise geologic time scales 2016*. 1st edn. Amsterdam: Elsevier, 234–240.

Pedersen, T. F., and Calvert, S. E. (1990). Anoxia vs. productivity: what controls the formation of organic-carbon-rich sediments and sedimentary rocks. *AAPG Bull.* 74 (4), 454–466. doi:10.1306/0c9b232b-1710-11d7-8645000102c1865d

Schnyder, J., Ruffell, A., Deconinck, J. F., and Baudin, F. (2006). Conjunctive use of spectral gamma-ray logs and clay mineralogy in defining late Jurassic-early Cretaceous palaeoclimate change (dorset, UK). *Palaeogeogr. Palaeoclimatol. Palaeoecol.* 229, 303–320. doi:10.1016/j.palaeo.2005.06.027

Shan, C., Zhang, T., Wei, Y., and Zhang, Z. (2017). Shale gas reservoir characteristics of Ordovician-Silurian formations in the central yangtze area, China. *Front. Earth Sci.* 11 (1), 184–201. doi:10.1007/s11707-016-0565-4

Shu, Y., Lu, Y., Chen, L., Wang, C., and Zhang, B. (2019). Factors influencing shale gas accumulation in the Lower Silurian longmaxi formation between the north and south jiaoshiba area, southeast sichuan basin, China. *Mar. Petroleum Geol.* 111, 905–917. doi:10.1016/j.marpetgeo.2019.06.029

Svensen, H. H., Hammer, Ø., and Corfu, F. (2015). Astronomically forced cyclicity in the Upper Ordovician and U–Pb ages of interlayered tephra, Oslo region,

Norway. *Palaeogeogr. Palaeoclimatol. Palaeoecol.* 418, 150–159. doi:10.1016/j.palaeo.2014.11.001

Talley, L. (2013). Closure of the global overturning circulation through the Indian, Pacific, and southern oceans: schematics and transports. *Oceanography* 26 (1), 80–97. doi:10.5670/oceanog.2013.07

Tenchov, G. G. (1997). Theoretical study of gamma ray index (igr): shale content (vsh) relationship for shaly sands. *J. For.* 13 (6), 685–691.

Thomson, D. J. (1982). Spectrum estimation and harmonic analysis. *Proc. IEEE* 70, 1055–1096. doi:10.1109/proc.1982.12433

Waltham, D. (2015). Milankovitch period uncertainties and their impact on cyclostratigraphy. *J. Sediment. Res.* 85 (8), 990–998. doi:10.2110/jsr.2015.66

Wang, D. S., Liu, Y., Zhang, J. C., Lang, Y., Li, Z., Tong, Z. Z., et al. (2022). Controls on marine primary productivity variation and organic matter accumulation during the late ordovician-early Silurian transition. *Mar. Petroleum Geol.* 142, 105742. doi:10.1016/j.marpetgeo.2022.105742

Wang, Y., Xinjing, L. I., Wang, H., Jiang, S., Dai, B., Ma, J., et al. (2019). Developmental characteristics and geological significance of the bentonite in the Upper Ordovician wufeng-lower Silurian longmaxi formation in eastern sichuan basin, sw China. *Petroleum Explor. Dev.* 46 (4), 687–700. doi:10.1016/S1876-3804(19)60226-0

Wei, X., Deng, Y., Yan, D., Liu, E., Jiang, P., Zhou, J., et al. (2023). Organic matter enrichment in Asia's palaeolake controlled by the early and middle Eocene global warming and astronomically driven precessional climate. *Mar. Petroleum Geol.* 154, 106342. doi:10.1016/j.marpetgeo.2023.106342

Wei, X., Yan, D., Luo, P., Jiang, P., Wang, H., Zhou, J., et al. (2020). Astronomically forced climate cooling across the Eocene–Oligocene transition in the pearl river mouth basin, northern South China Sea. *Palaeogeogr. Palaeoclimatol. Palaeoecol.* 558, 109945. doi:10.1016/j.palaeo.2020.109945

Wei, X., Yan, D., Wang, D., and Fu, H. (2024). Astronomically forced paleoclimate and sea-level changes recorded in the Continental margin of the South China Sea over the past ~23 m.y. *Geol. Soc. Am. Bull.* 136, 3553–3568. doi:10.1130/B37285.1

Williams, G. E. (1991). Milankovitch-band cyclicity in bedded halite deposits contemporaneous with late ordovician-early Silurian glaciation, canning basin, Western Australia. *Earth Planet. Sci. Lett.* 103, 143–155. doi:10.1016/0012-821x(91)90156-c

Wu, S. C., Chen, L., Xiong, M., Chen, X., Wang, G. X., Tan, X. C., et al. (2024). Depositional conditions of shale lithofacies during the late ordovician-early Silurian in the upper yangtze area, SW China: responses to sea-level changes. *Mar. Petroleum Geol.* 161, 106696. doi:10.1016/j.marpetgeo.2024.106696

Zhang, R., Jin, Z., Li, M., Gillman, M., Chen, S., Liu, Q., et al. (2023). Long-term periodicity of sedimentary basins in response to astronomical forcing: review and perspective. *Earth-Science Rev.* 244, 104533. doi:10.1016/j.earscirev.2023.104533

Zhang, X., Zhang, T., Lei, B., Zhang, J., and Yong, J. (2020). A giant sandy sediment drift in early Silurian (telychian) and its multiple sedimentological prosess. *Mar. Petroleum Geol.* 113, 104077. doi:10.1016/j.marpetgeo.2019.104077

Zhang, X., Zhang, T. S., Zhao, X. M., Zhu, H. H., Popa, M. E., Chen, L., et al. (2021). Effects of astronomical orbital cycle and volcanic activity on organic carbon accumulation during late ordovician-early Silurian in the upper yangtze area, south China. *Petroleum Explor. Dev.* 48 (4), 850–863. doi:10.1016/S1876-3804(21)60071-X

Zhong, Y., Wu, H., Fan, J., Fang, Q., Shi, M., Zhang, S., et al. (2019). Late Ordovician obliquity-forced glacio-eustasy recorded in the yangtze block, south China. *Palaeogeogr. Palaeoclimatol. Palaeoecol.* 540, 109520. doi:10.1016/j.palaeo.2019.109520

Zhong, Y. Y., Wu, H. C., Zhang, Y. D., Zhang, S. H., Yang, T. S., Li, H. Y., et al. (2018). Astronomical calibration of the middle Ordovician of the yangtze block, south China. *Palaeogeogr. Palaeoclimatol. Palaeoecol.* 505, 86–99. doi:10.1016/j.palaeo.2018.05.030

Zhu, H., Zhang, T., Liang, X., Zhang, Z., and Zhang, L. (2018). Insight into the pore structure of wufeng-longmaxi Black shales in the south sichuan basin, China. *J. Petroleum Sci. Eng.* 171, 1279–1291. doi:10.1016/j.petrol.2018.08.061